



# Abn-BLIP: Abnormality-aligned Bootstrapping Language-Image Pre-training for Pulmonary Embolism Diagnosis and Report Generation from CTPA

Zhusi Zhong<sup>a,b</sup>, Yuli Wang<sup>c</sup>, Lulu Bi<sup>a,b</sup>, Zhuoqi Ma<sup>a,b</sup>, Sun Ho Ahn<sup>a,b</sup>, Christopher J. Mullin<sup>a,b</sup>, Colin F. Greineder<sup>c</sup>, Michael K. Atalay<sup>a,b</sup>, Scott Collins<sup>a,b</sup>, Grayson L. Baird<sup>a,b</sup>, Cheng Ting Lin<sup>d</sup>, Webster Stayman<sup>c</sup>, Todd M. Kolb<sup>f</sup>, Ihab Kamel<sup>g</sup>, Harrison X. Bai<sup>d</sup>, Zhicheng Jiao<sup>a,b,\*</sup>

<sup>a</sup>Department of Diagnostic Imaging, Brown University Health, Providence 02903, USA

<sup>b</sup>Warren Alpert Medical School of Brown University, Providence 02903, USA

<sup>c</sup>Department of Biomedical Engineering, Johns Hopkins University School of Medicine, Baltimore 21205, USA

<sup>d</sup>Department of Radiology and Radiological Sciences, Johns Hopkins University School of Medicine, Baltimore 21205, USA

<sup>e</sup>Department of Emergency Medicine and Department of Pharmacology, University of Michigan, Ann Arbor 48109, USA

<sup>f</sup>Johns Hopkins University Division of Pulmonary and Critical Care Medicine, Baltimore 21205, USA

<sup>g</sup>Department of Radiology, University of Colorado School of Medicine, Aurora 80045, USA

## ARTICLE INFO

Article history:

Keywords:

Radiology report generation

Contrastive learning

3D medical image

Pulmonary embolism

## ABSTRACT

Medical imaging plays a pivotal role in modern healthcare, with computed tomography pulmonary angiography (CTPA) being a critical tool for diagnosing pulmonary embolism and other thoracic conditions. However, the complexity of interpreting CTPA scans and generating accurate radiology reports remains a significant challenge. This paper introduces Abn-BLIP (Abnormality-aligned Bootstrapping Language-Image Pre-training), an advanced diagnosis model designed to align abnormal findings to generate the accuracy and comprehensiveness of radiology reports. By leveraging learnable queries and cross-modal attention mechanisms, our model demonstrates superior performance in detecting abnormalities, reducing missed findings, and generating structured reports compared to existing methods. Our experiments show that Abn-BLIP outperforms state-of-the-art medical vision-language models and 3D report generation methods in both accuracy and clinical relevance. These results highlight the potential of integrating multimodal learning strategies for improving radiology reporting. The source code is available at <https://github.com/zzs95/abn-blip>.

© 2025 Elsevier B. V. All rights reserved.

## 1. Introduction

Pulmonary Embolism (PE) is a life-threatening condition caused by blood clots obstructing the pulmonary arteries, often leading to severe complications, long-term morbidity, and a high risk of mortality (Bělohlávek et al., 2013). Accurate and timely diagnosis is crucial for effective treatment and patient survival (Alonso-Martínez et al., 2010; Hendriksen et al.,

2017; Cahan et al., 2023). Computed tomography pulmonary angiography (CTPA) is the most widely used imaging modality for PE diagnosis, offering high sensitivity and specificity (Stein et al., 2006). However, traditional radiological interpretation of CTPA scans is labor-intensive, subject to inter-reader variability, and dependent on the expertise of the radiologist (Singh et al., 2011). Given the increasing clinical workload, the risk of missed or delayed diagnoses remains a significant concern.

Recent advancements in medical image AI have demonstrated significant potential in enhancing PE diagnosis and detection on CTPA scans (Soffer et al., 2021). AI-driven models,

\*Corresponding author.

E-mail: [zhicheng\\_jiao@brown.edu](mailto:zhicheng_jiao@brown.edu) (Z. Jiao).

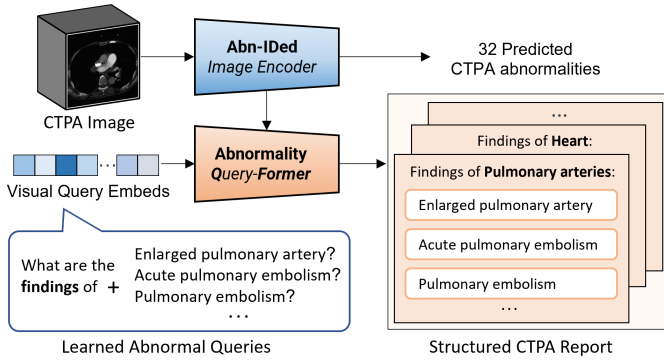


**Fig. 1. Abn-BLIP: a CTPA abnormality identification and structured report generation pipeline.** The Abn-IDed image encoder predicts 32 CTPA abnormalities and extracts abnormality-identified features. The learned visual queries interrogate CTPA scans by Abn-QFormer to extract the corresponding abnormal findings. These queries help generate a structured CTPA report, categorizing abnormalities under relevant organ-specific sections, such as pulmonary arteries and the heart.

particularly deep learning techniques leveraging multi-modal data, have been developed to automate embolism identification, quantify clot burden, and stratify patient risk (Huang et al., 2020; Liu et al., 2020; Zhong et al., 2024a). These methodologies improve diagnostic efficiency and provide a standardized evaluation framework to mitigate inter-reader variability. However, despite these advancements, many AI models primarily generate probabilistic predictions with limited interpretability, thereby limiting their reliability in clinical decision-making (Huang et al., 2020; Huang et al.; Lindenmeyer et al., 2024). By utilizing the vascular spatial structure, Tajbakhsh et al. (2019) summarize 3D contextual information around an embolus for assessment, ensuring consistent alignment and supporting data augmentation. Pu et al. (2023) apply segmentation of both intra- and extra-pulmonary arteries, partition identify suspicious by thresholding based on size and shape. Most existing AI solutions are predominantly centered on embolism detection rather than a comprehensive assessment of CTPA study, such as cardiac function, clot burden distribution, and ancillary thoracic findings.

To provide comprehensive assessment, vision-language models (VLMs) present a promising avenue for improving CTPA-based PE assessment by integrating imaging data with textual descriptions, enhancing both interpretability and clinical decision support (Zhong et al., 2024b). Medical VLMs bridge the gap between AI-generated findings and human-readable diagnostic reports, aligning with radiologists' workflows to streamline diagnosis and reduce variability (Nazi and Peng, 2024; Hartsock and Rasool, 2024; Tanno et al., 2024). Furthermore, vision-language methods facilitate automated report generation, providing structured insights and associated disease diagnosis (Jin et al., 2024). By incorporating multimodal data, such as clinical scores and patient history, VLMs can offer a more holistic assessment, improving patient management and risk stratification (Zhong et al., 2024c). Unlike conventional deep learning models that focus solely on classification or segmentation, VLMs generate comprehensive, human-readable

reports directly from imaging data, thereby enhancing interpretability and clinical utility (Wu et al., 2023; Bai et al., 2024). By bridging imaging findings with textual descriptions, these models facilitate a more intuitive and transparent AI-driven diagnostic process, ultimately improving clinical adoption and trust (Huang et al., 2023).

Despite these advantages, existing medical VLMs, while effective in general medical imaging tasks, exhibit limitations when applied specifically to CTPA-based PE assessment (Hager et al., 2024; Zhong et al., 2024b). Most current VLMs are trained on heterogeneous datasets encompassing a broad spectrum of medical images and general medical knowledge, leading to suboptimal performance in PE detection due to a lack of domain-specific expertise (Zhong et al., 2024b). Their capacity to handle complex reports and multi-abnormality queries is constrained, limiting their ability to integrate visual, textual, and clinical information in a manner comparable to expert radiologists (Hartsock and Rasool, 2024). More critically, these models often struggle to accurately capture subtle radiological findings essential for differentiating PE severity. The key challenge, therefore, lies in developing a PE-specific VLM that not only achieves high diagnostic accuracy but also enhances interpretability, aligns with radiologists' reporting conventions, and effectively integrates multimodal clinical data for comprehensive decision support.

To overcome these limitations, we propose the Abnormality-aligned Bootstrapping Language-Image Pretraining (Abn-BLIP) model, which enhances CTPA report generation by integrating abnormality recognition with structured abnormality descriptions, as illustrated in Fig. 1. Abnormality-aligned Contrastive Learning (ACL) reinforces the alignment between radiological features and medical textual findings, particularly in relation to disease severity. By strengthening the link between visually queried abnormal patterns and their corresponding textual descriptions, ACL improves the capacity to capture clinically significant findings. In comparison to case-level contrastive learning, our approach leverages anomaly- and organ-specific visual attention to establish more nuanced image-text associations. The diagnosis-driven reporting framework structures abnormality-specific visual queries into organized study findings, enabling a multi-stage diagnostic workflow for CTPA report generation. This structured reporting paradigm enhances interpretability, systematically organizes diagnostic assessments, and improves the clinical applicability of AI-generated radiology reports.

The key contributions can be summarized as follows:

- We integrate multi-label abnormality recognition to enhance diagnostic accuracy in CTPA report generation, optimizing hierarchical analysis, particularly in the pulmonary artery region.
- The abnormality-aligned contrastive learning framework enables fine-grained disease-level alignment, reducing redundant normal descriptions and improving the representation of rare and complex diseases.
- Abn-QFormer's visual querying mechanism dynamically refines information retrieval, mimicking a clinician's per-

spective by adaptively aggregating multi-scale image-text features.

- Guided by medical diagnostic principles, the framework models hierarchical relationships between anatomical regions and abnormalities, ensuring comprehensive and clinically meaningful CTPA reports.

## 2. Related work

**Image captioning:** Recent advancements in image captioning have transitioned from early encoder–decoder frameworks, where convolutional neural networks (CNNs) extracted visual features and recurrent neural networks (RNNs) generated textual descriptions (Vinyals *et al.*, 2015; Chen *et al.*, 2015). The incorporation of attention mechanisms refined these models by dynamically focusing on salient image regions, mitigating the limitations of fixed-length representations (Xu, 2015; Lu *et al.*, 2017). The adoption of Transformer architectures (Vaswani, 2017) further advanced the field by enhancing long-range dependency modeling and enabling parallel processing, leading to significant improvements in the fluency, coherence, and contextual accuracy of generated captions (Cornia *et al.*, 2020).

**Vision language pre-training:** More recently, Vision-Language Pre-Training (VLP) has leveraged contrastive learning to align images and text by mapping paired inputs into a shared embedding space (Radford *et al.*, 2021). Contrastive learning, a self-supervised technique, optimizes similarity and dissimilarity representations between positive and negative pairs (Khosla *et al.*, 2020). Early VLP models, such as CLIP (Radford *et al.*, 2021), employed contrastive losses (e.g., InfoNCE) to maximize mutual information between paired image-text inputs, enabling robust zero-shot and few-shot learning. However, these approaches often neglect intra-modal relationships and fine-grained structural information, which are critical in domains requiring subtle semantic distinctions.

Recent VLP frameworks address these limitations by integrating intra-modal contrastive learning and prefix-based language modeling, allowing the joint extraction of both global and localized features (Wang *et al.*, 2021). Transformer-based architectures now capture long-range dependencies and complex cross-modal interactions, as demonstrated in SimVLM (Wang *et al.*, 2021) and BLIP (Li *et al.*, 2023a). These advancements significantly enhance the contextual understanding of vision-language models, improving their effectiveness in downstream tasks such as image captioning, visual question answering, and medical abnormality detection.

**2D medical report generation:** Generating medical reports from radiological images is a specialized form of image captioning that requires structured, detailed descriptions of abnormalities, their locations, and clinical significance (Rehman *et al.*, 2024). Early approaches employed CNN-RNN and LSTM architectures to detect diseases in chest X-rays (Shin *et al.*, 2016) and generate structured medical reports (Yuan *et al.*, 2019; Yin *et al.*, 2019).

Recent advancements leverage Transformer-based decoders to improve medical report generation. A curriculum learning

framework utilizing an easy-to-hard strategy enhanced model efficiency with limited medical data and reduced reporting bias (Liu *et al.*, 2022). Additionally, a memory-driven Transformer decoder incorporating relational memory improved the completeness and accuracy of medical terminology in generated reports (Chen *et al.*, 2020). However, these models often lacked explicit integration of prior medical knowledge. To address this, Tanida *et al.* (2023) introduced a regional visual feature-based prompting mechanism for object detector-guided sentence-wise report generation, while Jin *et al.* (2024) employed a disease classification branch with token-based prompts to enhance clinical relevance. Despite these improvements, structured medical knowledge integration remains an ongoing challenge. Hou *et al.* (2023) proposed incorporating a predefined medical knowledge graph, leveraging cross-modal contrastive learning to capture relationships among medical findings.

**3D medical report generation:** Compared to 2D imaging, 3D modalities such as CT and MRI offer a more comprehensive assessment of a patient’s condition (Müller, 2002). However, the volumetric nature of these images necessitates sophisticated algorithms, particularly given the scarcity of paired 3D medical imaging datasets with corresponding reports (Li *et al.*, 2023b). To address this, Hamamci *et al.* (2024) introduced a Transformer with memory attention for generating detailed radiology reports from 3D chest CT volumes. Expanding contrastive learning in vision-language pretraining, Chen and Hong (2024) aligned 3D medical images with 2D pretrained vision-language models using BLIP’s generative capabilities.

Despite these advances, aligning representations solely at the image level remains inadequate for capturing the complexity of radiology reports, where distinguishing subtle pathological variations—e.g., pneumonia versus pulmonary embolism—is significantly more challenging than differentiating natural image categories (Wang *et al.*, 2022). Furthermore, the absence of clearly defined positive and negative pairs limits the effectiveness of contrastive learning for abnormality identification, highlighting the need for more advanced strategies in structured 3D medical report generation.

## 3. Methods

Based on clinical diagnostic guidelines for CTPA (Tan *et al.*, 2022; Bukhari *et al.*, 2024), we identified the necessity of a systematic framework to enhance abnormality detection and structured report generation for PE diagnosis. Accordingly, we developed a hierarchical diagnostic framework informed by the clinical expertise of radiologists from Brown University, Johns Hopkins University, and the University of Michigan, in collaboration with emergency physicians and pulmonologists. Their combined clinical insights ensured the framework’s clinical relevance, consistency, and generalizability across diverse healthcare settings.

As illustrated in Figure 2, the framework systematically structures the diagnostic process through a hierarchical evaluation of seven anatomical regions and 32 critical CTPA abnormalities. Within this structured approach, abnormalities are identified at a regional level and synthesized into a comprehen-

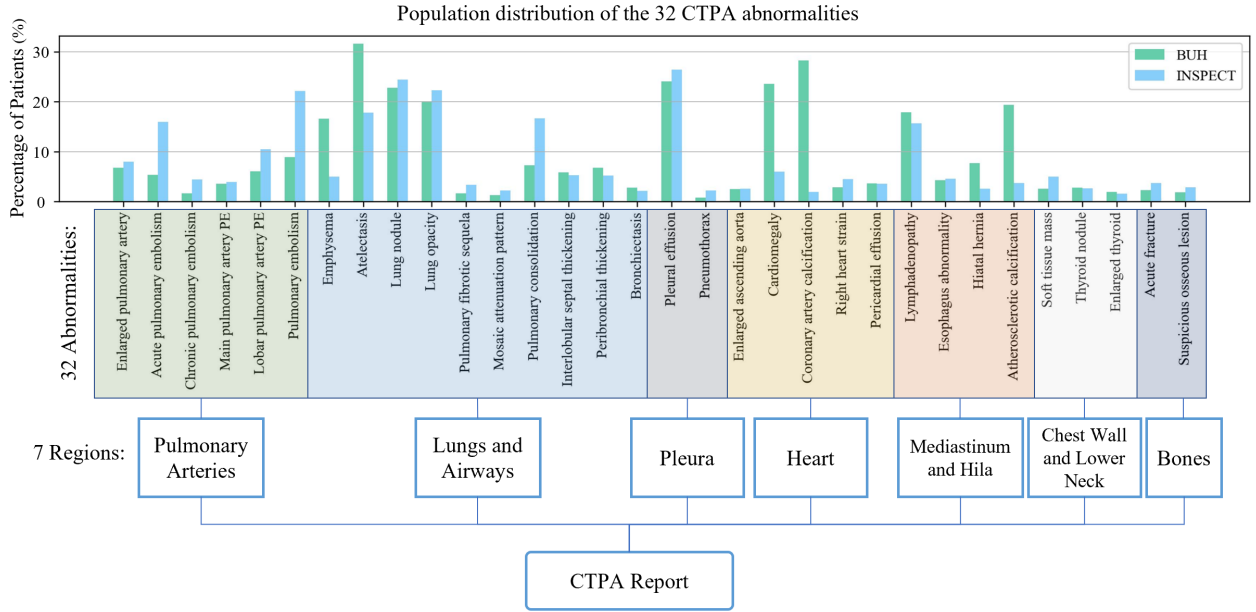


**Fig. 2.** The figure illustrates the population distribution of 32 CTPA abnormalities across two datasets (BUH and INSPECT), categorized into 7 anatomical regions: Pulmonary Arteries, Lungs and Airways, Pleura, Heart, Mediastinum and Hila, Chest Wall and Lower Neck, and Bones. This hierarchical framework facilitates comprehensive abnormality detection and enhances the generation of clinically meaningful CTPA reports. The abnormality labels were extracted from radiology reports using a large language model (LLM), enabling a multi-dimensional assessment of inter-regional variations across the datasets.

sive diagnostic summary, facilitating precise abnormality localization and standardized.

For diagnostic model training and report generation, CTPA radiology reports are processed using a large language model (LLM) (Dubey et al., 2024) to extract training targets. The LLM identifies 32 abnormality labels  $Y$  and retrieves their corresponding text-based findings  $T$ , ensuring an accurate representation of binary and textual findings.

### 3.1. Anatomy-guided multi-abnormality identification

Multi-abnormality identification in medical imaging is crucial for diagnosing and monitoring the 32 abnormalities observed in CTPA scans. Unlike single-label approaches, which detect only one abnormality, multi-label classification enables the simultaneous identification of co-occurring conditions (Ge et al., 2024), enhancing the understanding of the visual and critical relationships in cardiac and pulmonary abnormalities. As illustrated by the orange pathway of module (a) in Figure 3, Stage 1 involves training an image encoder and a multi-label classifier to detect abnormalities from CTPA images. Given an input scan  $x_l$ , the classifier predicts the probability  $P_k$  for each abnormality class  $k$ .

The image encoder architecture is based on an inflated 3D (I3D) ResNet152, which extends its 2D counterpart by inflating convolutional kernels into the temporal domain (Carreira and Zisserman, 2017). This preserves the pretrained 2D spatial representations while capturing spatiotemporal dependencies in CTPA sequences. The model consists of an initial  $7 \times 7 \times 3$  convolutional layer followed by a max pooling layer, maintaining the residual connections of ResNet152 for hierarchical feature extraction. The final residual layer outputs a feature map of dimensions  $2048 \times 7 \times 7 \times 10$ , which undergoes 3D adaptive

average pooling and a 3D convolutional layer to generate logits for 32 abnormality classes. The probabilities are computed using a sigmoid activation function, and the model is trained with a binary cross-entropy loss:

$$L_{\text{cls}} = - \sum_{k=1}^{32} y_k \log P_k + (1 - y_k) \log(1 - P_k) \quad (1)$$

where  $y_k$  denotes the ground-truth label of  $Y$ . Optimizing  $L_{\text{cls}}$  enables the model to learn robust multi-abnormality representations for comprehensive disease assessment.

To enhance visual feature representation for abnormality querying, multi-scale features ( $f_l^i \in \mathbb{R}^{C \times H_i \times W_i}$ ,  $l \in [1, 5]$ ) are extracted from five ResLayers of I3D ResNet. A 3D patch-pooling module partitions each scale into  $7 \times 7 \times 10$  non-overlapping sub-volumes. By applying average pooling to each small patch, the spatially aggregating of the pooled features reduced the spatial resolution while ensuring localized spatial and semantic information retention. The pooled features of each scale are further embedded through 3D convolution blocks with ReLU activation and batch normalization, reducing their dimensionality to  $C'_l \times d_v$ , where  $d_v$  represents the visual feature dimension. These multi-scale embeddings are concatenated into a unified feature representation with  $M$  channels.

To integrate visual and semantic abnormality information, the predicted multi-class probabilities  $P$  are embedded via a linear layer into the visual feature space as  $F_{\text{CLS}}$ . The resulting abnormality-aware embedding is concatenated with the aggregated visual embeddings, yielding a joint representation of visual features  $\mathbf{v}$  in  $\mathbb{R}^{(M+1) \times d_v}$ , where  $(M+1)$  is the number of concatenated visual tokens.

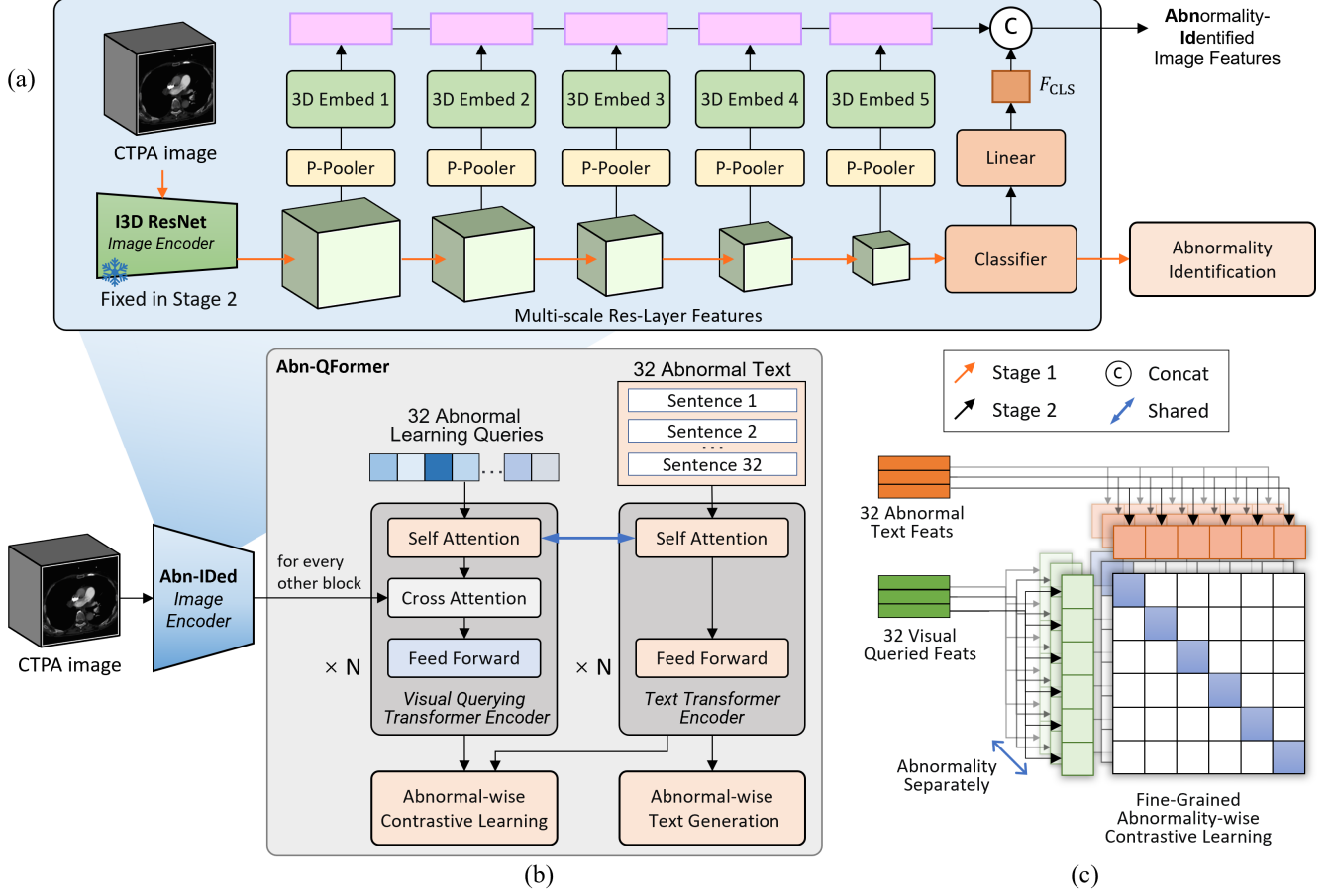


**Fig. 3.** Overview of the proposed Abn-BLIP model for CTPA abnormality diagnosis and report generation. (a) Anatomy-guided multi-abnormality identification in Stage 1: Multi-scale abnormality-identified image feature extraction for transformer encoders. (b) Abnormality-driven visual Querying Transformers (Abn-QFormer): Joint optimization of two objectives, enforcing abnormal queries (a set of learnable embeddings) to extract visual abnormal representations most relevant to their corresponding abnormal text descriptions. (c) Abnormality-aligned Contrastive Learning (ACL): Achieving more fine-grained visual queried representations by aligning abnormalities.

### 3.2. Abnormality-driven visual querying transformers

We propose an Abnormality-driven visual Querying Transformers (Abn-QFormer) module designed to generate abnormality descriptions by aligning abnormality-specific visual features with disease-level text findings, as illustrated in module (b) of Figure 3.

The Abn-QFormer consists of two distinct submodules tailored for textual and visual information processing. The text transformer employs a Self-Attention (SA) mechanism, functioning as both an encoder and decoder for textual representations. The visual querying transformer extends this design by incorporating both Self-Attention (SA) and Cross-Attention (CA) layers, facilitating interactions with visual features and generating contextual embeddings for 32 predefined abnormalities. To leverage prior knowledge, the Self-Attention modules in both submodules are initialized with pre-trained BERT-base weights (Devlin, 2018), while the CA layers are randomly initialized to adapt specifically to visual learning.

For the  $k$ -th abnormality, the textual input is represented as a tokenized sequence  $\mathbf{T}^k = [t_1, t_2, \dots, t_L]$ , where  $L$  is the number of tokens. Each token is embedded into a fixed-dimensional vector and processed by a Multi-Head Self-Attention (MHSA)

mechanism, which computes pairwise attention weights across all tokens:

$$\text{SA}(\mathbf{X}) = \text{softmax}\left(\frac{\mathbf{X}\mathbf{W}_Q\mathbf{X}\mathbf{W}_K^T}{\sqrt{d_k}}\right)\mathbf{X}\mathbf{W}_V \quad (2)$$

where  $\mathbf{W}_Q$ ,  $\mathbf{W}_K$ , and  $\mathbf{W}_V$  are learnable projection matrices,  $d_k$  is the dimensionality of the query and key vectors. The output of the attention layer is refined through a feed-forward network (FFN):

$$\text{FFN}(\mathbf{X}) = \text{ReLU}(\mathbf{X}\mathbf{W}_1 + \mathbf{b}_1)\mathbf{W}_2 + \mathbf{b}_2 \quad (3)$$

To stabilize training, residual connections and layer normalization are applied:

$$\begin{aligned} \mathbf{H}^l &= \text{LayerNorm}(\mathbf{H}^{l-1} + \text{MHSA}(\mathbf{H}^{l-1})) \\ \mathbf{H}^l &= \text{LayerNorm}(\mathbf{H}^l + \text{FFN}(\mathbf{H}^l)) \end{aligned} \quad (4)$$

The final layer [CLS] token embedding  $\mathbf{h}$  serves as the global textual representation, encapsulating high-level semantic information.

The visual querying transformer extends textual processing by incorporating 32 learnable query embeddings:

$$\mathbf{Q}_{\text{abn}} = [\mathbf{Q}_1, \mathbf{Q}_2, \dots, \mathbf{Q}_{32}], \mathbf{Q}_i \in \mathbb{R}^{1 \times d} \quad (5)$$

Each query is a trainable parameter that extracts abnormality-relevant features from visual embeddings. The Self-Attention layers facilitate intra-query interactions, capturing contextual relationships among queries, while the Cross-Attention layers enable dynamic interactions with visual features  $\mathbf{v}$ , effectively aligning the queried attention with the corresponding abnormalities:

$$\text{CA}(\mathbf{X}, \mathbf{v}) = \text{softmax}\left(\frac{\mathbf{X}\mathbf{W}_Q(\mathbf{v}\mathbf{W}_K)^T}{\sqrt{d_k}}\right)(\mathbf{v}\mathbf{W}_V) \quad (6)$$

where  $\mathbf{X}$  represents the updated query embeddings.  $\mathbf{W}_Q$ ,  $\mathbf{W}_K$ , and  $\mathbf{W}_V$  are learnable projection matrices of CA layers.

The Multi-Head Cross-Attention (MHCA) layers enhance the queries' ability to selectively attend to abnormality-relevant visual regions. The model combines self-attention and cross-attention to capture intra-query dependencies and cross-modal alignments, refining query embeddings across layers. The iterative querying process is defined as:

$$\begin{aligned} \mathbf{Z}^l &= \text{LayerNorm}(\mathbf{Z}^{l-1} + \text{MHSA}(\mathbf{Z}^{l-1})) \\ \mathbf{Z}^l &= \text{LayerNorm}(\mathbf{Z}^l + \text{MHCA}(\mathbf{Z}^l, \mathbf{v})) \\ \mathbf{Z}^l &= \text{LayerNorm}(\mathbf{Z}^l + \text{FFN}(\mathbf{Z}^l)) \end{aligned} \quad (7)$$

A shared transformer backbone between textual and visual modules enhances parameter efficiency and supports diverse cross-modal tasks. The encoder uses bi-directional self-attention for representation learning, while the decoder applies causal self-attention for sequence generation. Embedding layers, cross-attention layers, and feed-forward networks (FFN) remain consistent across encoding and decoding tasks.

### 3.3. Fine-grained bootstrapping language-image pre-training for visual querying

Our abnormality-driven training framework leverages image-text pairs to optimize two complementary objectives: Abnormality-aligned Contrastive Learning (ACL) and Abnormal Image-Grounded Text Generation (ATG). These objectives facilitate fine-grained cross-modal alignment and bootstrapping of the model's capability to generate abnormality-specific descriptions.

ACL aims to maximize mutual information between image and text representations by aligning their embeddings within a shared feature space. This approach refines cross-modal understanding by associating abnormality-specific visual queries with corresponding textual descriptions. Specifically, ACL utilizes 32 visual query embeddings ( $\mathbf{Z}$ ) from the transformer-based visual encoder and 32 [CLS] token embeddings ( $\mathbf{h}$ ) from the text encoder, ensuring robust cross-modal representation learning.

The alignment process employs contrastive loss to optimize both image-to-text and text-to-image similarities. For the  $k$ -th

abnormality, the Image-to-text alignment is formalized as:

$$\mathcal{L}_{\text{I2T}}^k = -\frac{1}{N} \sum_{i=1}^N \text{softmax}(P_k) \log \frac{\exp(\Phi(\mathbf{Z}_i^k, \mathbf{h}_i^k)/\tau)}{\sum_{j=1}^N \exp(\Phi(\mathbf{Z}_i^k, \mathbf{h}_j^k)/\tau)} \quad (8)$$

where  $N$  represents the batch size,  $\Phi$  represents cosine similarity, and  $\tau$  is a temperature scaling factor.  $P^k$  denotes the predicted anomaly probabilities serving as soft labels for cross-modal alignment.  $\mathbf{Z}^k$  and  $\mathbf{h}^k$  represents the normalized visual and textual embeddings of  $k$ -th abnormality. The corresponding text-to-image loss is defined analogously:

$$\mathcal{L}_{\text{T2I}}^k = -\frac{1}{N} \sum_{i=1}^N \text{softmax}(P_k) \log \frac{\exp(\Phi(\mathbf{h}_i^k, \mathbf{Z}_i^k)/\tau)}{\sum_{j=1}^N \exp(\Phi(\mathbf{h}_i^k, \mathbf{Z}_j^k)/\tau)} \quad (9)$$

The final ACL loss aggregates bidirectional contrastive losses across all 32 abnormalities, as shown in (c) of Figure 3 ensuring a balanced alignment between modalities:

$$\mathcal{L}_{\text{ACL}} = \frac{1}{2} \sum_{k=1}^{32} (\mathcal{L}_{\text{I2T}}^k + \mathcal{L}_{\text{T2I}}^k) \quad (10)$$

To maintain modality-specific information and prevent feature leakage, we introduce unimodal self-attention masks, ensuring independent refinement of visual queries and text embeddings. Additionally, freezing the image encoder during training improves efficiency by leveraging in-batch negatives for enhanced negative sampling.

ATG trains the abnormal querying transformer to generate textual descriptions conditioned on visual inputs, enabling Abn-QFormer to convert abnormality-related visual features into coherent textual findings. The extracted visual abnormalities using learned queries are propagated to text tokens via self-attention layers with multimodal causal masks. This structured attention mechanism enforces information flow such that queries interact only among themselves, while text tokens attend to both queries and prior textual context.

The text generation follows an autoregressive decoding paradigm, using a special [DEC] token to initialize the sequence. For the  $k$ -th abnormality, the probability of generating the text sequence  $\mathbf{T}^k = [t_1, t_2, \dots, t_L]$  given queried visual embedding  $\mathbf{Z}^k$  is:

$$P_{\text{ATG}}^k(\mathbf{T}|\mathbf{Z}) = \prod_{i=1}^L P(t_i|t_{<i}, \mathbf{Z}) \quad (11)$$

where  $t_i$  represents the  $i$ -th token in the sequence, and  $t_{<i}$  denotes its preceding tokens. The model is trained with cross-entropy loss to maximize the likelihood of the generated text:

$$\mathcal{L}_{\text{ATG}} = -\frac{1}{N} \sum_{n=1}^N \sum_{k=1}^{32} \sum_{j=1}^L \log P_{\text{ATG}}^k(t_j^n|t_{<j}^n, \mathbf{Z}^n) \quad (12)$$

To enhance generalization and mitigate overfitting, we apply label smoothing with a factor of 0.1.

By jointly optimizing ACL and ATG alongside multi-label abnormality classification, our pre-training framework ensures robust cross-modal alignment while maintaining the flexibility to generate detailed abnormality descriptions.

### 3.4. Inference for study report

For abnormality description generation, Abn-QFormer employs an encoder-decoder architecture with cross-modal attention mechanisms to align visually queried features with tokenized textual outputs, generating 32 distinct abnormality descriptions.

To construct a comprehensive CTPA findings report, we integrate a large language model (LLM) that systematically organizes abnormality-specific descriptions across seven anatomical regions, synthesizing them into a cohesive final report. For patients undergoing multiple scans with varying imaging parameters, a LLaMA3-based report-writing agent (Dubey *et al.*, 2024) aggregates and summarizes abnormality-specific observations at the regional level (Supplementary Appendix .4). To ensure clinical adherence and emphasize key diagnostic insights, tailored prompt engineering is employed in a structured radiology format .

## 4. Experiments and results

### 4.1. Datasets

To evaluate the effectiveness of the proposed method across multiple clinical tasks, we conducted experiments on two CTPA datasets with corresponding radiology reports: (1) INSPECT (Huang *et al.*, 2023) from Stanford University and (2) CTPA Imaging Data from Brown University Health (BUH).

The INSPECT dataset (Huang *et al.*, 2023), collected at Stanford Medicine between 2000 and 2021, comprises 23,248 CTPA scans from 19,402 patients at risk for PE. It includes the impression sections of radiology reports, providing radiologist-generated diagnostic descriptions and interpretations.

At BUH, a retrospective study was conducted, identifying patients who underwent CTPA imaging between 2015 and 2019, including those with multiple follow-up scans. The dataset contains 59,754 image-report pairs from 19,565 patients. The two datasets were combined and split into training, validation, and testing sets in a 7:1:2 ratio.

#### 4.1.1. Image preprocessing

CTPA scans were preprocessed by extracting pixel data from DICOM files, standardizing spatial coordinates, and normalizing Hounsfield Units (HU). To enhance anatomical focus, lung regions were segmented and cropped with a 20 mm margin (Hofmanninger *et al.*, 2020). Axial images were resampled to 1.5 mm in-plane resolution and 3 mm out-of-plane resolution, then padded and cropped to  $224 \times 224 \times 160$ . HU values were normalized to  $[0, 1]$  by clipping values outside the -1000 to 1000 range.

#### 4.1.2. Report preprocessing

We employed LLaMA3 (Dubey *et al.*, 2024) for report preprocessing, including text cleaning and abnormality label annotation. The "Findings" sections were extracted as the primary diagnostic content. To facilitate region-specific analysis, free-text findings were reformatted into a structured seven-organ framework using a standardized prompting strategy (detailed in Supplementary Appendix .1).

We leveraged the language model's medical reasoning capabilities to automatically extract binary anomaly labels and corresponding textual descriptions for 32 CTPA abnormalities from the "Findings" sections (detailed in Supplementary Appendix .2 and Appendix .3). The extracted labels served as ground-truth references for training and evaluating multi-abnormality diagnosis models, ensuring consistency in classification. Additionally, the corresponding textual descriptions provided detailed abnormality context, improving the interpretability of structured reports. To further understand the dataset composition, we analyzed the population distributions of these abnormalities, as visualized in Figure 2.

### 4.2. Implementation details

The training process consists of two stages. In the first stage, a multi-abnormality identification model is trained by optimizing the parameters of an I3D ResNet-based image encoder, enabling it to learn discriminative features for detecting multiple abnormalities. In the second stage, the image encoder is frozen, and the remaining components, including multi-scale image feature embeddings and multimodal transformer layers in Abn-QFormer, are trained to refine abnormality-specific semantic representations.

For each input CTPA image, the image encoder generates multi-scale feature embeddings with abnormality probability distributions of size  $257 \times 1408$ . The Abn-QFormer module employs 32 learnable queries, each corresponding to a specific abnormality with a feature dimension of 768. These queries extract 32 distinct abnormality-specific visual features, each represented as a 256-dimensional vector, capturing fine-grained abnormality patterns.

The transformer backbone consists of 12 hidden layers to support robust multimodal fusion. Training and validation are conducted on two NVIDIA RTX A6000 GPUs. The model is optimized using AdamW with a learning rate of  $1 \times 10^{-5}$ , a batch size of 20, and a maximum of 27 epochs, ensuring stable convergence and optimal performance.

### 4.3. Abnormality diagnosis results

We assess Abn-BLIP's diagnostic performance using accuracy (ACC), area under the receiver operating characteristic curve (AUC), sensitivity (Sen) and specificity (Spe). Table 2 presents a comparative analysis of our proposed method against state-of-the-art (SOTA) approaches for CTPA abnormality classification. We specifically benchmarked our model against leading medical VLMs. As representative VLMs tailored for 3D medical imaging, we selected M3D (Bai *et al.*, 2024) and RadFM (Wu *et al.*, 2023), which employ visual question-answering (VQA) for abnormality detection. In these evaluations, the VLMs used 32 structured prompts, each querying a specific abnormality in the format:

"Is there any indication of <Anomaly name> in this image? (This is a true or false question, please answer 'Yes' or 'No')."

Among the compared models, M3D achieved an ACC of 0.895 but performed poorly in terms of AUC (0.499), sensitivity (0.011), and F1-score (0.479), indicating a strong bias towards

**Table 1. Comparison of the proposed model with current 3D medical VLM and report generation methods on both testing sets with respect to NLG metrics. The highest performances are highlighted in bold.**

Datasets		BUH						INSPECT					
Methods	Prompt	BL-1	BL-4	RG-1	RG-L	MT	BERT-F1	BL-1	BL-4	RG-1	RG-L	MT	BERT-F1
RadFM (Wu et al., 2023)	cap	0.178	0.017	0.159	0.099	0.148	0.825	0.136	0.007	0.105	0.077	0.091	0.827
RadFM (Wu et al., 2023)	cap + region	0.208	0.097	0.270	0.222	0.411	0.845	0.375	0.207	0.358	0.331	0.481	0.871
RadFM (Wu et al., 2023)	cap + region + oneshot	0.209	0.099	0.261	0.209	0.374	0.826	0.389	0.223	0.399	0.355	0.471	0.853
M3D (Bai et al., 2024)	cap	0.170	0.010	0.136	0.090	0.104	0.817	0.081	0.003	0.088	0.068	0.061	0.807
M3D (Bai et al., 2024)	cap + region	0.192	0.025	0.208	0.125	0.190	0.825	0.162	0.015	0.142	0.103	0.116	0.787
M3D (Bai et al., 2024)	cap + region + oneshot	0.219	0.074	0.164	0.125	0.158	0.826	0.101	0.038	0.122	0.104	0.100	0.822
MedBlip (Chen and Hong, 2024)	contrastive Learning	0.109	0.069	0.179	0.144	0.279	0.829	0.250	0.203	0.393	0.344	0.514	0.892
CT2Rep (Hamamci et al., 2024)	memory-driven	0.188	0.003	0.410	0.384	0.382	0.821	0.140	0.003	<b>0.678</b>	<b>0.677</b>	0.519	0.862
Abn-BLIP (Ours)	contrastive Learning	<b>0.525</b>	<b>0.349</b>	<b>0.504</b>	<b>0.440</b>	<b>0.550</b>	<b>0.910</b>	<b>0.652</b>	<b>0.532</b>	0.630	0.588	<b>0.704</b>	<b>0.937</b>

**Table 2. Comparison of current 3D medical VLMs on a combined testing set using multi-label classification metrics. The highest performances are highlighted in bold.**

Methods	ACC	AUC	Sen.	Spe.	F1
M3D (Bai et al., 2024)	0.895	0.499	0.011	<b>0.987</b>	0.479
RadFM (Wu et al., 2023)	0.480	0.495	<b>0.485</b>	0.500	0.303
Abn-BLIP (Ours)	<b>0.896</b>	<b>0.773</b>	0.384	0.932	<b>0.653</b>

**Table 3. Comparison of PE diagnosis performance.**

Methods	ACC	AUC	Sen.	Spe.	F1
M3D (Bai et al., 2024)	0.795	0.500	0.003	<b>0.997</b>	0.446
RadFM (Wu et al., 2023)	0.549	0.490	0.390	0.590	0.468
PENet (Huang et al., 2020)	0.212	0.513	<b>0.984</b>	0.015	0.183
Abn-BLIP (Ours)	<b>0.838</b>	<b>0.732</b>	0.274	0.982	<b>0.656</b>

negative cases and limited capacity for detecting abnormalities. RadFM exhibited the weakest overall performance, with an ACC of 0.480, AUC of 0.495, sensitivity of 0.485, specificity of 0.500, and an F1-score of 0.303, suggesting insufficient discriminatory power. In contrast, our proposed approach achieved the highest AUC (0.773) and F1-score (0.653), along with an ACC of 0.896, sensitivity of 0.384, and specificity of 0.932. These results highlight our method’s enhanced ability to capture fine-grained abnormality features, leading to more precise and reliable CTPA abnormality detection.

For PE diagnosis comparison in Table 3, M3D exhibited high specificity (0.997) but extremely low sensitivity (0.003), indicating a strong bias toward negative cases. RadFM achieved more balanced sensitivity (0.390) and specificity (0.590) but showed limited overall performance (ACC: 0.549, AUC: 0.490). PENet (Huang et al., 2020) attained the highest sensitivity (0.984) but suffered from excessive false positives (specificity: 0.015, ACC: 0.212), likely due to significant distribution differences in its training data with a tendency toward high-risk predictions. Abn-BLIP demonstrated the most robust performance, achieving the highest ACC (0.838), AUC (0.732), and F1-score (0.656), along with a strong specificity

(0.982). While its sensitivity (0.274) remains moderate, it effectively balances false positives and false negatives, making it a more reliable approach for PE diagnosis in CTPA analysis.

#### 4.4. CTPA report generation results

We compare Abn-BLIP against SOTA medical VLMs and 3D medical report generation frameworks. Given the sensitivity of report generation to prompt design, we explored various prompting strategies to optimize VLM performance. Specifically, we evaluate multiple prompts (see Supplementary Appendix 5), including general captioning, organ-specific lists, and one-shot examples designed to elicit targeted abnormality descriptions. Additionally, we compare with representative 3D medical report generation models, CT2Rep (Hamamci et al., 2024) and MedBlip (Chen and Hong, 2024), which leverage contrastive learning and memory-driven frameworks for cross-domain image-to-report generation.

We assess the quality of the generated reports using a range of Natural Language Generation (NLG) metrics to compare model outputs with reference texts. Specifically, we used BLEU (Bilingual Evaluation Understudy) to evaluate fluency and adequacy based on n-gram overlap (Lin and Och, 2004), ROUGE (Recall-Oriented Understudy for Gisting Evaluation) to assess content overlap for summarization (Lin, 2004), METEOR (Metric for Evaluation of Translation with Explicit Ordering) to incorporate unigram matching, semantic similarity, and morpheme analysis (Banerjee and Lavie, 2005), and BERTScore, which leverages pre-trained language model embeddings to measure semantic similarity (Zhang\* et al., 2020).

Table 1 presents model performance on the testing data of BUH and INSPECT datasets, evaluated using BLEU (BL-1, BL-4), ROUGE (RG-1, RG-L), METEOR (MT), and BERT F1-score. Across both datasets, Abn-BLIP outperformed all baselines, demonstrating its superior ability to generate clinically relevant, well-structured reports. On the BUH dataset, Abn-BLIP achieved a BLEU-1 score of 0.525, BLEU-4 of 0.349, ROUGE-1 of 0.504, ROUGE-L of 0.440, and a BERT F1-score of 0.910. On the INSPECT dataset, it attained a BLEU-1 score of 0.652, BLEU-4 of 0.532, ROUGE-1 of 0.630, ROUGE-L of



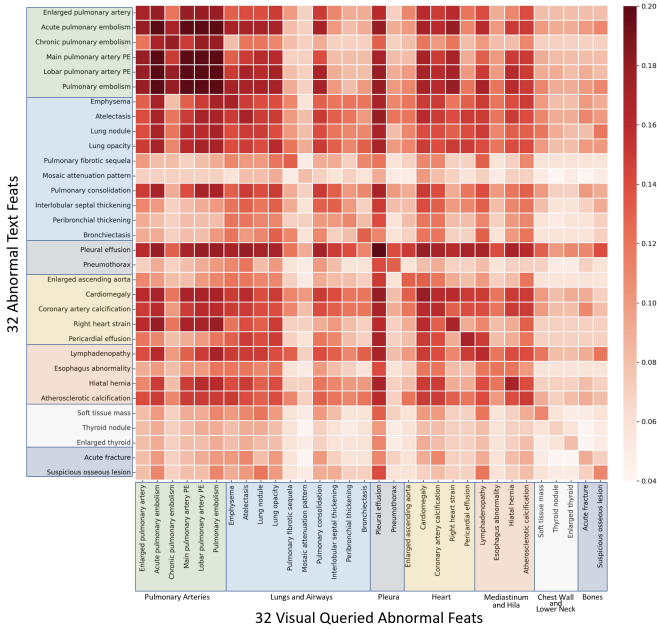


**Fig. 4.** Visualization of cross-modal cosine similarity heatmap between textual and visual features of 32 distinct CTPA abnormalities. The textual features are derived from the text descriptions of each abnormality, while the visual features are the queried representations on the corresponding images. Each cell in the heatmap indicates the similarity score between a specific abnormality’s textual and visual representation, providing insights into the alignment between the two modalities.

0.588, and a BERT F1-score of 0.937, reinforcing its robustness across diverse datasets.

VLM-based models demonstrated varying performance, with M3D and RadFM benefiting from regional prompts and one-shot learning strategies. Among them, RadFM outperforms M3D in BLEU-4 and ROUGE metrics, indicating a stronger ability to capture detailed disease descriptions. Despite optimized prompting, their performance remained inferior to Abn-BLIP, indicating challenges in generating structured and clinically coherent reports.

Supervised learning-based models, MedBlip and CT2Rep, achieve competitive performance, surpassing VLMs in most cases. Notably, CT2Rep achieves the highest ROUGE-1 score (0.678) and ROUGE-L score (0.677) on the INSPECT dataset, indicating strong summarization capabilities for key imaging findings. However, both models struggle with generating well-structured, long-form reports, constraining their overall performance improvements. In contrast, Abn-BLIP effectively synthesizes detailed, structured findings, ensuring both clinical relevance and linguistic coherence, achieving state-of-the-art performance in automated radiology report generation.

4.5. Image-text correlation for abnormalities

Figure 4 presents a heatmap of cross-modal cosine similarity between textual and visual features for 32 distinct CTPA abnormalities, providing insights into their anatomical relationships. Notably, high similarity scores are observed in the Pulmonary Arteries, Heart, and specific Lung and Airway regions, reflecting their vascular interdependence. Pulmonary arteries mediate

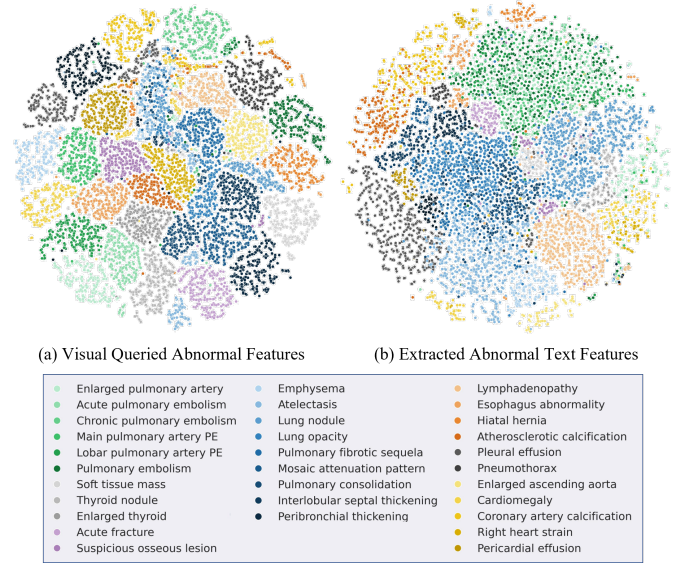


**Fig. 5.** t-SNE visualization of normalized image and text features for abnormalities. Each colored point represents one of 32 detected abnormalities, from 20,000 randomly sampled features. (a) The abnormal image features were extracted using visual querying, guided by learned abnormality-wise queries from the visual querying transformer encoder. (b) The abnormal text features were encoded by a text transformer encoder based on descriptive sentences of the abnormalities.

blood flow between the heart and lungs, highlighting the clinical significance of PE-related abnormalities.

Localized high-intensity diagonal clusters within the Pulmonary Arteries Region indicate strong intra-regional alignment. Abnormalities like “acute pulmonary embolism” and “pulmonary embolism” (including “main pulmonary artery PE” and “lobar pulmonary artery PE”) exhibit high similarity, consistent with their shared vascular etiology. In contrast, “chronic pulmonary artery embolism” shows lower similarity to acute PE variants, underscoring distinct pathophysiological processes. Acute PE typically manifests with sudden vascular obstruction and hemodynamic instability, whereas chronic PE develops progressively with subtler radiographic manifestations.

“Pleural effusion” demonstrates exhibits moderate similarity, with off-diagonal patterns suggesting feature overlap with Lungs and Airways due to anatomical proximity. This reflects shared radiographic characteristics, as pleural effusions often co-occur with pulmonary abnormalities, emphasizing the need for contextual inter-regional analysis in diagnostic frameworks.

Conversely, abnormalities in the Chest Wall, Lower Neck, and Bone regions exhibit lower similarity scores. Conditions such as “suspicious osseous lesion” and “thyroid nodule” show low similarity with vascular and pulmonary abnormalities, reflecting distinct diagnostic contexts. Their reduced similarity may stem from focus on non-vascular structures and lower clinical prevalence in PE-related assessments.

Overall, these findings underscore the critical role of vascular structures in PE diagnosis and the importance of cross-modal feature alignment in understanding inter-regional relationships in CTPA analysis.

Ground Truth	Abn-BLIP (Ours)	CT2Rep	MedBLIP
<p><b>Study 1</b> Pulmonary arteries: <i>Pulmonary embolus</i> in the distal left main pulmonary artery with <i>clot</i> extending into lobar distribution predominantly in the left lower lobe. <i>Significant clot</i> in the right main pulmonary artery and upper and lower lobar pulmonary arteries. Lungs and Airways: <i>Airspace disease</i> in the right lower lung.</p> <p>Pleura: Normal. Heart: Flattening of the interventricular septum and <i>dilatation of the right ventricle</i>; <i>RV : LV = 1.5</i>.</p> <p>Mediastinum and Hila: Normal. Chest Wall and Lower Neck: Normal. Chest Bones: No acute abnormality.</p>	<p>Pulmonary arteries: Multiple <i>bilateral pulmonary emboli</i> are observed, with a <i>large clot burden</i> extending into the lobar and segmental branches of both lungs.</p> <p>Lungs and Airways: A 4 mm <i>subpleural nodule</i> is present in the right upper lobe. <i>Minimal dependent atelectasis</i> is observed. Wedge-shaped <i>peripheral consolidation</i> is noted in the right lower lobe.</p> <p>Pleura: Normal. Heart: <i>Right ventricular dilatation</i> with septal bowing and right heart strain is present, indicating mild to moderate right ventricular enlargement and increased prominence. Mediastinum and Hila: Normal. Chest Wall and Lower Neck: Normal. Chest Bones: Normal.</p>	<p><b>Study 1</b> pulmonary arteries <b>normal</b>. lungs and airways <b>normal</b>. pleura normal. heart <b>normal</b>. mediastinum and hila normal. chest wall and lower neck normal. chest bones no acute abnormality.</p>	<p>Pulmonary arteries: <b>Normal</b>. Lungs and Airways: <b>Normal</b>. Pleura: <b>Normal</b>. Heart: <b>Normal</b>. Mediastinum and Hila: <b>Normal</b>. Chest Wall and Lower Neck: <b>Normal</b>. Chest Bones: No acute abnormality.</p>
<p><b>Study 2</b> Pulmonary arteries: There is poor opacification of the pulmonary arterial vasculature. A <i>filling defect</i> is seen involving a subsegmental branch of the left upper lobe pulmonary artery, which probably represents an <i>acute pulmonary embolus</i>.</p> <p>Lungs and Airways: Extensive <i>bilateral cystic bronchiectasis</i> is noted involving both lungs, more pronounced towards the lung bases, with suggestion of a few fluid levels within some of the larger cavities, not significantly changed from previous. Tree in bud opacities are present throughout both lower lobes, probably not dissimilar from previous when accounting for differences in study technique. This is suggestive of a small airways disease process.</p> <p>Pleura: Normal. Heart: Normal. Mediastinum and Hila: Several <i>mildly enlarged mediastinal lymph nodes</i> are present, unchanged. Chest Wall and Lower Neck: Normal. Chest Bones: Normal.</p>	<p>Pulmonary arteries: Multiple <i>filling defects</i> are noted involving subsegmental branches of the left upper lobe pulmonary artery, likely representing <i>acute pulmonary emboli</i>.</p> <p>Lungs and Airways: <i>Bilateral cystic bronchiectasis</i> is noted involving both lungs, more pronounced towards the lung bases, with suggestion of a few fluid levels within some of the larger cavities.</p> <p>Pleura: Normal. Heart: Normal. Mediastinum and Hila: <i>Mildly enlarged mediastinal lymph nodes</i> are present. Chest Wall and Lower Neck: Normal. Chest Bones: Normal.</p>	<p><b>Study 2</b> pulmonary arteries <b>normal</b>. lungs and airways <b>normal</b>. pleura normal. heart <b>normal</b>. mediastinum and hila normal. chest wall and lower neck normal. chest bones no acute abnormality.</p>	<p>Pulmonary arteries: <b>Normal</b>. Lungs and Airways: <b>Normal</b>. Pleura: <b>Normal</b>. Heart: <b>Normal</b>. Mediastinum and Hila: <b>Normal</b>. Chest Wall and Lower Neck: <b>Normal</b>. Chest Bones: No acute abnormality.</p>
		RadFM	M3D
		<p><b>Study 1</b> Pulmonary arteries, Lungs and Airways: Subsegmental <i>pulmonary embolism</i> in both lower lobes. <i>Emphysema</i>. Mild pulmonary edema. <i>Bibasilar atelectasis</i>. Heart: Normal. Mediastinum and Hila: <i>Mild cardiomegaly</i>. Enlarged main pulmonary artery to 3.4 cm. Chest Wall and Lower Neck: Normal. Chest Bones: <i>Status post left thoracotomy</i>.</p>	No Output
		<p><b>Study 2</b> 1. Mild pulmonary edema. 2. <i>Subsegmental pulmonary embolism</i> in both lower lobes. 3. 18 mm focal groundglass nodule in the left lower lobe. 4. 7.5 x 4.4 x 3.4 cm <i>expansile lucent lesion in the left posterior ninth rib</i>.</p>	Pulmonary artery 3.4 cm. Left lower lobe nodule 18 mm. 6 mm left hilar node.

**Fig. 6. Examples of the generated reports. Our results are compared with the ground truth, the 3D report generation methods and medical VLM methods. The blue italic text is the correct predictions corresponding to the actual reports, and the red areas indicate the untrue information in the predictions.**

#### 4.6. Visualization of abnormal representation

Figure 5 presents a t-SNE visualization of learned representations for visual (a) and textual (b) features across 32 distinct CTPA abnormalities, to evaluate their clustering patterns and separability. Each point represents a feature vector, with colors representing different abnormality categories.

The t-SNE plot of visual features (a) demonstrates distinct clusters among related abnormalities. For example, PE-associated abnormalities ("Enlarged pulmonary artery," "Acute pulmonary embolism," and "Chronic pulmonary embolism") cluster closely, as do lung parenchymal abnormalities ("Lung nodule," "Lung opacity," and "Pulmonary consolidation"). This indicates that visual features effectively capture morphological and textural patterns specific to each category.

The t-SNE plot of textual features (b) shows tighter clustering at the organ level, with notable groupings in the Lungs and Airways (blue) and Pulmonary Arteries (green). This indicates that textual descriptions within an organ share similarities, though some abnormalities, such as "Enlarged pulmonary artery," "Lymphadenopathy," "Esophagus abnormality," and "Atherosclerotic calcification," are well-separated, reflecting their distinct semantic characteristics.

Comparing the two plots, visual features show greater separability, indicating that learnable queries enhance feature discrimination. However, both modalities exhibit strong discriminative capabilities, underscoring the value of integrating visual and textual features for a comprehensive abnormality characterization.

#### 4.7. Qualitative analysis

Figure 6 illustrates a comparative case study of radiology reports generated by the proposed Abn-BLIP model, existing 3D report generation methods (CT2Rep, MedBLIP), and medical VLMs (RadFM, M3D) against the ground truth. The evaluation includes two representative cases, each highlighting distinct anatomical regions and pathological findings.

The reports of Abn-BLIP closely align with the ground truth, accurately identifying key pulmonary and cardiac abnormalities. It effectively detects bilateral pulmonary emboli with a large clot burden (Study 1) and multiple filling defects indicative of acute pulmonary embolism (Study 2). Additionally, it captures subpleural nodules and peripheral consolidation (Study 1) and offers a detailed characterization of bilateral cystic bronchiectasis with fluid levels (Study 2). Cardiac findings, including right ventricular dilatation (Study 1) and mildly enlarged mediastinal lymph nodes (Study 2), align well with the ground truth, underscoring Abn-BLIP's superior anatomical and pathological specificity.

In contrast, 3D report generation methods show notable limitations. CT2Rep and MedBLIP exhibit severe underreporting, frequently misclassifying abnormalities as "normal" across multiple organ systems. Their low sensitivity, particularly in detecting critical conditions like pulmonary embolism, renders their outputs clinically unreliable.

Medical VLMs exhibit variability in performance. RadFM correctly identifies pulmonary embolism, mild pulmonary edema, and cardiomegaly but fails to detect bronchiectasis and

introduces a potentially incorrect finding (status post left thoracotomy). M3D lacks robustness, failing to generate output for Study 1. While it identifies pulmonary artery enlargement and lymphadenopathy in Study 2, it misses acute pulmonary embolism and cystic bronchiectasis, indicating limited diagnostic coverage.”

#### 4.8. Ablation study

To evaluate the effectiveness of the proposed architectural components, we conducted ablation studies focusing on multi-scale feature fusion and the abnormal prediction embedding ( $F_{CLS}$ ).

Table 4 presents multi-label abnormality classification results. Using only the fifth residual layer (L5) features without  $F_{CLS}$  established a strong baseline, achieving an accuracy of 0.894, AUC of 0.772, sensitivity of 0.393, specificity of 0.930, and F1-score of 0.652. Adding  $F_{CLS}$  slightly improved the F1-score (0.653) with minimal impact on other metrics, indicating a minor but positive contribution. Multi-scale feature fusion alone led to modest improvements across all metrics (e.g., F1-score: 0.654), highlighting its effectiveness in enhancing feature representation. However, integrating both did not yield further gains, with sensitivity decreasing (0.384) and F1-score unchanged (0.653), suggesting  $F_{CLS}$  adds limited value when multi-scale features are present for diagnosis.

For report generation, Table 5 examined abnormality- and study-level descriptions. Using L5 features alone resulted in weaker text generation, with a BLEU-1 of 0.414, BLEU-4 of 0.050, ROUGE-L of 0.647, METEOR of 0.632, and BERT-F1 of 0.952. Incorporating  $F_{CLS}$  significantly improved all metrics (e.g., BLEU-1: 0.623, ROUGE-L: 0.828), demonstrating its role in generating more descriptive and semantically relevant reports. Multi-scale features alone further enhanced performance (e.g., BLEU-1: 0.672, ROUGE-L: 0.874), and the highest scores were achieved when both components were combined with BLEU-1 reaching 0.677, BLEU-4 increasing to 0.112, METEOR improving to 0.831, and BERT-F1 peaking at 0.983.

A similar trend was observed for study-level findings, where L5 features alone yielded weaker results with BLEU-1 at 0.424, BLEU-4 at 0.092, and ROUGE-L at 0.491. Incorporating  $F_{CLS}$  improved contextual understanding raising BLEU-1 to 0.523 and ROUGE-L to 0.684. Multi-scale features alone further boosted performance with BLEU-1 increasing to 0.590 and BLEU-4 to 0.446, and their combination yielded the best performance, with BLEU-1 at 0.594 and ROUGE-L at 0.872.

These findings underscore the benefits of multi-scale feature fusion in both classification and report generation. While  $F_{CLS}$  enhances feature representation, its impact on classification is limited when multi-scale features are present. However, it significantly improves report descriptiveness and coherence, highlighting the value of hierarchical feature integration and contextual embedding in medical image analysis.

#### 4.9. Discussion

While the Abn-BLIP model has shown strong potential in diagnosing abnormalities from CTPA scans and generating re-

**Table 4. Ablation studies for abnormality multi-label classification.**

Img-Feat	$F_{CLS}$	ACC	AUC	Sen.	Spe.	F1
L5 only	-	0.894	0.772	<b>0.393</b>	0.930	0.652
L5 only	✓	0.895	0.772	0.387	0.931	0.653
Multi-scale	-	0.896	0.773	0.387	0.932	<b>0.654</b>
Multi-scale	✓	<b>0.896</b>	<b>0.773</b>	0.384	<b>0.932</b>	0.653

**Table 5. Ablation studies for report generation.**

Ablations		Abnormality level description					
Img-Feat	$F_{CLS}$	BL-1	BL-4	RG-1	RG-L	MT	BERT-F1
L5 only	-	0.414	0.050	0.649	0.647	0.632	0.952
L5 only	✓	0.623	0.096	0.828	0.826	0.788	0.977
Multi-scale	-	0.672	0.107	0.866	0.865	0.825	0.982
Multi-scale	✓	<b>0.677</b>	<b>0.112</b>	<b>0.874</b>	<b>0.873</b>	<b>0.831</b>	<b>0.983</b>

Ablations		Study level findings					
Img-Feat	$F_{CLS}$	BL-1	BL-4	RG-1	RG-L	MT	BERT-F1
L5 only	-	0.424	0.292	0.491	0.428	0.614	0.907
L5 only	✓	0.577	0.430	0.574	0.522	0.639	0.925
Multi-scale	-	0.581	0.431	0.571	0.519	0.639	0.925
Multi-scale	✓	<b>0.594</b>	<b>0.446</b>	<b>0.578</b>	<b>0.527</b>	<b>0.641</b>	<b>0.926</b>

ports, several challenges remain. The predefined abnormality-based reporting framework enables structured image analysis and reduces missed findings; however, it may limit the detection of novel or rare conditions, potentially leading to diagnostic omissions due to its limited capacity for detecting predefined or unseen conditions. Further validation across broader modalities is essential for disease detection tasks to comprehensively assess its effectiveness.

The model also exhibits inconsistencies in abnormality classification and report generation, necessitating further research to enhance reliability and diagnostic coverage. Integrating diverse visual features with advanced attention mechanisms Le Vuong and Kwak (2025), and graph-based representations Hou et al. (2023) could improve its capacity to capture complex relationships among abnormalities beyond predefined categories. Addressing biases in training data, including demographic imbalances and disease prevalence, is also crucial to improving fairness and generalizability.

The real-world clinical report data present greater challenges due to their complexity and specialized domain knowledge. The experiment revealed that current SOTA medical AI models remain insufficient for fully autonomous end-to-end report generation. Moreover, existing classification and NLG metrics may not adequately capture the clinical significance of detected abnormalities, highlighting the necessity for evaluation frameworks that integrate clinical outcomes and expert feedback to guide model improvement.

## 5. Conclusion

In conclusion, Abn-BLIP marks a major advancement in medical imaging interpretation through its sophisticated vision-

language model tailored for CTPA scans. By leveraging learnable queries and cross-modal attention mechanisms for CTPA abnormalities, the model achieves high accuracy in abnormality detection and generates comprehensive radiology reports outperforming existing approaches. The experimental results showed substantial improvements across key NLG metrics, underscoring its effectiveness. Qualitative visualizations further confirm the model's image-language capability in accurately capturing and describing critical pulmonary and cardiac abnormalities. Furthermore, a case study highlighted Abn-BLIP's ability to accurately identify both primary and incidental findings, which is a critical aspect of comprehensive patient care. While the model holds great promise in reducing diagnostic errors and enhancing clinical decision-making, future research should address its limitations, particularly regarding rare abnormalities and dependency on the predefined diagnosis framework. Overall, Abn-BLIP offers a structured approach to CTPA report generation enhancing diagnostic reliability and efficiency in healthcare.

### Declaration of competing interest

The authors declare that they have no known competing financial interests or personal relationships that could have appeared to influence the work reported in this paper.

### References

- Jan Bělohávek, Vladimír Dytrych, and Aleš Linhart. Pulmonary embolism, part i: Epidemiology, risk factors and risk stratification, pathophysiology, clinical presentation, diagnosis and nonthrombotic pulmonary embolism. *Experimental & Clinical Cardiology*, 18(2):129, 2013.
- José Luis Alonso-Martínez, FJ Annicchero Sánchez, and MA Urbieto Echezarreta. Delay and misdiagnosis in sub-massive and non-massive acute pulmonary embolism. *European journal of internal medicine*, 21(4):278–282, 2010.
- Janneke MT Hendriksen, Marleen Koster-van Ree, Marcus J Morgenstern, Ruud Oudega, Roger EG Schutgens, Karel GM Moons, and Geert-Jan Geersing. Clinical characteristics associated with diagnostic delay of pulmonary embolism in primary care: a retrospective observational study. *BMJ open*, 7(3):e012789, 2017.
- Noa Cahan, Eyal Klang, Edith M Marom, Shelly Soffer, Yiftach Barash, Evyatar Burshtein, Eli Konen, and Hayit Greenspan. Multimodal fusion models for pulmonary embolism mortality prediction. *Scientific Reports*, 13(1): 7544, 2023.
- Paul D Stein, Sarah E Fowler, Lawrence R Goodman, Alexander Gottschalk, Charles A Hales, Russell D Hull, Kenneth V Leeper Jr, John Popovich Jr, Deborah A Quinn, Thomas A Sos, et al. Multidetector computed tomography for acute pulmonary embolism. *New England Journal of Medicine*, 354(22):2317–2327, 2006.
- Satinder Singh, Paul Pinsky, Naomi S Fineberg, David S Gierada, Kavita Garg, Yanhui Sun, and P Hrudaya Nath. Evaluation of reader variability in the interpretation of follow-up ct scans at lung cancer screening. *Radiology*, 259(1):263–270, 2011.
- Shelly Soffer, Eyal Klang, Orit Shimon, Yiftach Barash, Noa Cahan, Hayit Greenspan, and Eli Konen. Deep learning for pulmonary embolism detection on computed tomography pulmonary angiogram: a systematic review and meta-analysis. *Scientific reports*, 11(1):15814, 2021.
- Shih-Cheng Huang, Tanay Kothari, Imon Banerjee, Chris Chute, Robyn L Ball, Norah Borus, Andrew Huang, Bhavik N Patel, Pranav Rajpurkar, Jeremy Irvin, et al. Penet—a scalable deep-learning model for automated diagnosis of pulmonary embolism using volumetric ct imaging. *NPJ digital medicine*, 3(1):61, 2020.
- Weifang Liu, Min Liu, Xiaojuan Guo, Peiyao Zhang, Ling Zhang, Rongguo Zhang, Han Kang, Zhenguo Zhai, Xincao Tao, Jun Wan, et al. Evaluation of acute pulmonary embolism and clot burden on ctpa with deep learning. *European radiology*, 30:3567–3575, 2020.
- Zhusi Zhong, Helen Zhang, Fayeze H Fayad, Andrew C Lancaster, John Sollee, Shreyas Kulkarni, Cheng Ting Lin, Jie Li, Xinbo Gao, Scott Collins, et al. Pulmonary embolism mortality prediction using multimodal learning based on computed tomography angiography and clinical data. *arXiv preprint arXiv:2406.01302*, 2024a.
- Shih-Cheng Huang, Anuj Pareek, Roham Zamanian, Imon Banerjee, and Matthew P Lungren. Multimodal fusion with deep neural networks for leveraging CT imaging and electronic health record: A case-study in pulmonary embolism detection. 10(1):22147. ISSN 2045-2322. doi: 10.1038/s41598-020-78888-w. URL <https://www.nature.com/articles/s41598-020-78888-w>.
- Adrian Lindenmeyer, Malte Blattmann, Stefan Franke, Thomas Neumuth, and Daniel Schneider. Inadequacy of common stochastic neural networks for reliable clinical decision support. *arXiv preprint arXiv:2401.13657*, 2024.
- Nima Tajbakhsh, Jae Y Shin, Michael B Gotway, and Jianming Liang. Computer-aided detection and visualization of pulmonary embolism using a novel, compact, and discriminative image representation. *Medical image analysis*, 58:101541, 2019.
- Jiantao Pu, Naciye Sinem Gezer, Shangsi Ren, Aylin Ozgen Alpaydin, Emre Ruhut Avci, Michael G Risbano, Belinda Rivera-Lebron, Stephen Yu-Wah Chan, and Joseph K Leader. Automated detection and segmentation of pulmonary embolisms on computed tomography pulmonary angiography (ctpa) using deep learning but without manual outlining. *Medical Image Analysis*, 89:102882, 2023.
- Zhusi Zhong, Yuli Wang, Jing Wu, Wen-Chi Hsu, Vin Somasundaram, Lulu Bi, Shreyas Kulkarni, Zhuoqi Ma, Scott Collins, Grayson L Baird, et al. Vision language model for report generation and outcome prediction in ct pulmonary angiogram. 2024b.
- Zabir Al Nazi and Wei Peng. Large language models in healthcare and medical domain: A review. In *Informatics*, volume 11, page 57. MDPI, 2024.
- Iryna Hartscock and Ghulam Rasool. Vision-language models for medical report generation and visual question answering: A review. *arXiv preprint arXiv:2403.02469*, 2024.
- Ryutarō Tanno, David GT Barrett, Andrew Sellergren, Sumedh Ghaisas, Samanth Dathathri, Abigail See, Johannes Welbl, Charles Lau, Tao Tu, Shekoofeh Azizi, et al. Collaboration between clinicians and vision-language models in radiology report generation. *Nature Medicine*, pages 1–10, 2024.
- Haibo Jin, Haoxuan Che, Yi Lin, and Hao Chen. Promptmrg: Diagnosis-driven prompts for medical report generation. In *Proceedings of the AAAI Conference on Artificial Intelligence*, volume 38, pages 2607–2615, 2024.
- Zhusi Zhong, Jie Li, John Sollee, Scott Collins, Harrison Bai, Paul Zhang, Terrence Healey, Michael Atalay, Xinbo Gao, and Zhicheng Jiao. Multi-modality regional alignment network for covid x-ray survival prediction and report generation. *arXiv preprint arXiv:2405.14113*, 2024c.
- Chaoyi Wu, Xiaoman Zhang, Ya Zhang, Yanfeng Wang, and Weidi Xie. Towards generalist foundation model for radiology. *arXiv preprint arXiv:2308.02463*, 2023.
- Fan Bai, Yuxin Du, Tiejun Huang, Max Q-H Meng, and Bo Zhao. M3d: Advancing 3d medical image analysis with multi-modal large language models. *arXiv preprint arXiv:2404.00578*, 2024.
- Shih-Cheng Huang, Zepeng Huo, Ethan Steinberg, Chia-Chun Chiang, Matthew P Lungren, Curtis P Langlotz, Serena Yeung, Nigam H Shah, and Jason A Fries. Inspect: a multimodal dataset for pulmonary embolism diagnosis and prognosis. *arXiv preprint arXiv:2311.10798*, 2023.
- Paul Hager, Friederike Jungmann, Robbie Holland, Kunal Bhagat, Inga Hubrecht, Manuel Knauer, Jakob Vielhauer, Marcus Makowski, Rickmer Braren, Georgios Kaissis, et al. Evaluation and mitigation of the limitations of large language models in clinical decision-making. *Nature medicine*, 30(9):2613–2622, 2024.
- Oriol Vinyals, Alexander Toshev, Samy Bengio, and Dumitru Erhan. Show and tell: A neural image caption generator. In *Proceedings of the IEEE conference on computer vision and pattern recognition*, pages 3156–3164, 2015.
- Xinlei Chen, Hao Fang, Tsung-Yi Lin, Ramakrishna Vedantam, Saurabh Gupta, Piotr Dollár, and C Lawrence Zitnick. Microsoft coco captions: Data collection and evaluation server. *arXiv preprint arXiv:1504.00325*, 2015.
- Kelvin Xu. Show, attend and tell: Neural image caption generation with visual

- attention. *arXiv preprint arXiv:1502.03044*, 2015.
- Jiasen Lu, Caiming Xiong, Devi Parikh, and Richard Socher. Knowing when to look: Adaptive attention via a visual sentinel for image captioning. In *Proceedings of the IEEE conference on computer vision and pattern recognition*, pages 375–383, 2017.
- A Vaswani. Attention is all you need. *Advances in Neural Information Processing Systems*, 2017.
- Marcella Cornia, Matteo Stefanini, Lorenzo Baraldi, and Rita Cucchiara. Meshed-memory transformer for image captioning. In *Proceedings of the IEEE/CVF conference on computer vision and pattern recognition*, pages 10578–10587, 2020.
- Alec Radford, Jong Wook Kim, Chris Hallacy, Aditya Ramesh, Gabriel Goh, Sandhini Agarwal, Girish Sastry, Amanda Askell, Pamela Mishkin, Jack Clark, et al. Learning transferable visual models from natural language supervision. In *International conference on machine learning*, pages 8748–8763. PMLR, 2021.
- Prannay Khosla, Piotr Teterwak, Chen Wang, Aaron Sarna, Yonglong Tian, Phillip Isola, Aaron Maschiot, Ce Liu, and Dilip Krishnan. Supervised contrastive learning. *Advances in neural information processing systems*, 33:18661–18673, 2020.
- Zirui Wang, Jiahui Yu, Adams Wei Yu, Zihang Dai, Yulia Tsvetkov, and Yuan Cao. Simvlm: Simple visual language model pretraining with weak supervision. *arXiv preprint arXiv:2108.10904*, 2021.
- Junnan Li, Dongxu Li, Silvio Savarese, and Steven Hoi. Blip-2: Bootstrapping language-image pre-training with frozen image encoders and large language models. In *International conference on machine learning*, pages 19730–19742. PMLR, 2023a.
- Marwareed Rehman, Imran Shafi, Jamil Ahmad, Carlos Osorio Garcia, Alina Eugenia Pascual Barrera, and Imran Ashraf. Advancement in medical report generation: current practices, challenges, and future directions. *Medical & Biological Engineering & Computing*, pages 1–22, 2024.
- Hoo-Chang Shin, Kirk Roberts, Le Lu, Dina Demner-Fushman, Jianhua Yao, and Ronald M Summers. Learning to read chest x-rays: Recurrent neural cascade model for automated image annotation. In *Proceedings of the IEEE conference on computer vision and pattern recognition*, pages 2497–2506, 2016.
- Jianbo Yuan, Haofu Liao, Rui Luo, and Jiebo Luo. Automatic radiology report generation based on multi-view image fusion and medical concept enrichment. In *Medical Image Computing and Computer Assisted Intervention—MICCAI 2019: 22nd International Conference, Shenzhen, China, October 13–17, 2019, Proceedings, Part VI 22*, pages 721–729. Springer, 2019.
- Changchang Yin, Buyue Qian, Jishang Wei, Xiaoyu Li, Xianli Zhang, Yang Li, and Qinghua Zheng. Automatic generation of medical imaging diagnostic report with hierarchical recurrent neural network. In *2019 IEEE international conference on data mining (ICDM)*, pages 728–737. IEEE, 2019.
- Fenglin Liu, Shen Ge, Yuexian Zou, and Xian Wu. Competence-based multimodal curriculum learning for medical report generation. *arXiv preprint arXiv:2206.14579*, 2022.
- Zhihong Chen, Yan Song, Tsung-Hui Chang, and Xiang Wan. Generating radiology reports via memory-driven transformer. *arXiv preprint arXiv:2010.16056*, 2020.
- Tim Tanida, Philip Müller, Georgios Kaissis, and Daniel Rueckert. Interactive and explainable region-guided radiology report generation. In *Proceedings of the IEEE/CVF Conference on Computer Vision and Pattern Recognition*, pages 7433–7442, 2023.
- Xiaodi Hou, Zhi Liu, Xiaobo Li, Xingwang Li, Shengtian Sang, and Yijia Zhang. Mkcl: Medical knowledge with contrastive learning model for radiology report generation. *Journal of Biomedical Informatics*, 146:104496, 2023.
- NL Müller. Computed tomography and magnetic resonance imaging: past, present and future. *European Respiratory Journal*, 19(35 suppl):3s–12s, 2002.
- Johann Li, Guangming Zhu, Cong Hua, Mingtao Feng, Basheer Bennamoun, Ping Li, Xiaoyuan Lu, Juan Song, Peiyi Shen, Xu Xu, et al. A systematic collection of medical image datasets for deep learning. *ACM Computing Surveys*, 56(5):1–51, 2023b.
- Ibrahim Ethem Hamamci, Sezgin Er, and Bjoern Menze. Ct2rep: Automated radiology report generation for 3d medical imaging. In *International Conference on Medical Image Computing and Computer-Assisted Intervention*, pages 476–486. Springer, 2024.
- Qiuhui Chen and Yi Hong. Medblip: Bootstrapping language-image pre-training from 3d medical images and texts. In *Proceedings of the Asian Conference on Computer Vision*, pages 2404–2420, 2024.
- Zifeng Wang, Zhenbang Wu, Dinesh Agarwal, and Jimeng Sun. Medclip: Contrastive learning from unpaired medical images and text. *arXiv preprint arXiv:2210.10163*, 2022.
- Stephanie Tan, John W Nance, Linda B Haramati, Prabhakar Rajiah, William M Sherk, Grégoire Le Gal, and Jadranka Stojanovska. Pulmonary cta reporting: Ajr expert panel narrative review. *American Journal of Roentgenology*, 218(3):396–404, 2022.
- Syed Muhammad Awais Bukhari, Joshua G Hunter, Kaustav Bera, Charit Tippareddy, Cody Reid Johnson, Shweta Ravi, Shashwat Chakraborti, Robert Chapman Gilkeson, and Amit Gupta. Clinical and imaging aspects of pulmonary embolism: a primer for radiologists. *Clinical Imaging*, page 110328, 2024.
- Abhimanyu Dubey, Abhinav Jauhri, Abhinav Pandey, Abhishek Kadian, Ahmad Al-Dahle, Aiesha Letman, Akhil Mathur, Alan Schelten, Amy Yang, Angela Fan, et al. The llama 3 herd of models. *arXiv preprint arXiv:2407.21783*, 2024.
- Xueren Ge, Abhishek Satpathy, Ronald Williams, John Stankovic, and Homa Alemzadeh. Dkec: Domain knowledge enhanced multi-label classification for diagnosis prediction. In *Proceedings of the 2024 Conference on Empirical Methods in Natural Language Processing*, pages 12798–12813, 2024.
- Joao Carreira and Andrew Zisserman. Quo vadis, action recognition? a new model and the kinetics dataset. In *proceedings of the IEEE Conference on Computer Vision and Pattern Recognition*, pages 6299–6308, 2017.
- Jacob Devlin. Bert: Pre-training of deep bidirectional transformers for language understanding. *arXiv preprint arXiv:1810.04805*, 2018.
- Johannes Hofmanninger, Florian Prayer, Jeanny Pan, Sebastian Röhrich, Helmut Prosch, and Georg Langs. Automatic lung segmentation in routine imaging is primarily a data diversity problem, not a methodology problem. *European Radiology Experimental*, 4(1):1–13, 2020.
- Chin-Yew Lin and Franz Josef Och. ORANGE: a method for evaluating automatic evaluation metrics for machine translation. In *COLING 2004: Proceedings of the 20th International Conference on Computational Linguistics*, pages 501–507. Geneva, Switzerland, aug 23–aug 27 2004. COLING. URL <https://www.aclweb.org/anthology/C04-1072>.
- Chin-Yew Lin. ROUGE: A package for automatic evaluation of summaries. In *Text Summarization Branches Out*, pages 74–81. Barcelona, Spain, July 2004. Association for Computational Linguistics. URL <https://www.aclweb.org/anthology/W04-1013>.
- Satanjeev Banerjee and Alon Lavie. METEOR: An automatic metric for MT evaluation with improved correlation with human judgments. In *Proceedings of the ACL Workshop on Intrinsic and Extrinsic Evaluation Measures for Machine Translation and/or Summarization*, pages 65–72. Ann Arbor, Michigan, June 2005. Association for Computational Linguistics. URL <https://www.aclweb.org/anthology/W05-0909>.
- Tianyi Zhang\*, Varsha Kishore\*, Felix Wu\*, Kilian Q. Weinberger, and Yoav Artzi. BERTscore: Evaluating text generation with bert. In *International Conference on Learning Representations*, 2020. URL <https://openreview.net/forum?id=SkeHuCVFDr>.
- Trinh Thi Le Vuong and Jin Tae Kwak. Moma: momentum contrastive learning with multi-head attention-based knowledge distillation for histopathology image analysis. *Medical Image Analysis*, 101:103421, 2025.

## Supplementary Material

### Appendix .1. Regional findings extraction prompt

#### LLM Prompt

You are a medical AI visual assistant that can analyze a single CT image. Unfortunately, you can't see the image but you can receive a diagnostic report of findings in the CT image. The report describes the findings in the image: <FINDINGS REPORT>

Your task is to extract the relevant information of "<REGION NAME>" from the report.

For the output finding content, try to keep the original text if given finding section matched in report.

If the given section is not matched but is mentioned, extract the content from related finding sections.

If the report section that is not mentioned in any other related finding sections, please output 'No finding.'

Please ensure that the information is accurate and concise, reflecting only what is mentioned in the report. The finding content should be extracted and presented clearly. Please be careful not to mention the doctor name and diagnosis time in report. Do not output prompts.

## Appendix .2. Abnormality label extraction prompt

**LLM Prompt**

You are a medical AI visual assistant that can analyze a single CT image. Unfortunately, you can't see the image but you can receive a diagnostic report of findings in the CT image. The report describes the findings in the image: <FINDINGS REPORT>

The 32 kinds of predefined abnormal findings are <ABNORMALITY LIST>

You are given a medical report and a list of medical abnormalities. Now, you are analyzing this report and your task is to determine whether each abnormality is mentioned in the report.

Conditions for marking abnormalities as "Yes" or "No":

- Yes (Abnormality Mentioned): If the abnormality is described in findings or impression sections of the report, please indicate "Yes" in the output JSON for that abnormality.
- No (Abnormality Not Mentioned): If an abnormality is not mentioned in any form within the report, indicate it as "No". If the report explicitly states that the patient does not have the abnormality or that it is ruled out, mark it as "No". If the information is unclear or ambiguous regarding the abnormality, still mark it as "No" to maintain accuracy and avoid false positives. Exclude mentions that are conditional or speculative, such as hypothetical statements or scenarios where the abnormality is not confirmed to be present.

It is a true or false question, please make sure that all your answers are only included one of "Yes" and "No". Please do NOT output the text described in the report, make sure the answer must be "Yes" or "No" only, do NOT include any text after the "Yes" or "No" answer.

Output format:

```
{
  "Finding 1": ["Yes" or "No"],
  "Finding 2": ["Yes" or "No"],
  ... (continue for other findings)
}
```

For example:

```
{
  "Chronic pulmonary embolism": "Yes",
  "Lung opacity": "No",
  ... (continue for other findings)
}
```

Fix the output to JSON format. Only return one corrected JSON.

Please make sure your answers are in the order and number of the 32 given predefined findings.

Please ensure that the information is accurate and concise, reflecting only what is mentioned in the report. Each finding should be extracted and presented clearly. Please be careful not to mention the file name and report.

*Appendix .3. Abnormality-wise finding extraction prompt***LLM Prompt**

You are a medical AI visual assistant that can analyze a single CT image. Unfortunately, you can't see the image but you can receive a diagnostic report of findings in the CT image. The report describes the findings in the image: <FINDINGS REPORT>

The task is to describe the "<ABN NAME>" in the image. The answer is based on the information of the CT imaging report, but from the perspective of images. Always ask questions and answer as if directly looking at the image.

The content described must be derived from the CT impact report. The answer should be a complete sentence, using clinical and professional expressions to describe the findings of "<ABN NAME>".

If the "<ABN NAME>" is presented normally or not mentioned at all in the report, simply output "No findings" as the answer.

Please ensure that the answers are accurate and concise. The requirements of truth and objectivity must be strictly adhered to, and there must be no fantasy or fabrication. The output content should be extracted and presented clearly. Please be careful not to mention dates, file names, and personal names.

Please do NOT output prompt text. Only output requires content of the given abnormality directly without explanation, or introduction. Output plain text.



*Appendix .4. Region-based report rewriting prompt***LLM Prompt**

You are a medical AI visual assistant that can analyze a single CT image. Unfortunately, you can't see the image but you can receive a diagnostic report of findings in the CT image. The <ABNORMALITY-WISE FINDINGS> are the findings of <REGION NAME> region in the image.

You are given a list of abnormality-specific descriptions of <REGION NAME> region in a medical image.

Please generalize them to a findings conclusion with concise, professional and medical terminology to describe the findings of the <REGION NAME> region.

Appropriately modify the expression to succinctly summarize the descriptions of similar diseases, the same organs, and the same tissues. Delete the same meaning or the same disease and repeated descriptions. Reduce the contradictory descriptions between abnormalities. Eliminate ambiguity caused by grammatical errors and repetitions.

Do NOT state the abnormality one by one, particularly a normal description such as "No abnormal xxxx are observed".

Output "Normal." as a conclusion if there is not any abnormality in this region. Otherwise, please output a sentence summary with a conclusion of the observed abnormalities.

Do NOT output prompt text (such as 'Here is the rewritten FINDINGS section:'). Only output findings content. Output plain text.

*Appendix .5. Image caption prompt for medical VLM***VLM Prompt**

# Image captioning

Please write a radiology report consisting of findings for this medical image.

# Organ list

Please include the findings of Pulmonary arteries, Lungs and Airways, Pleura, Heart, Mediastinum and Hila, Chest Wall and Lower Neck, Chest Bones

# One-shot example

For example:

FINDINGS:

Pulmonary arteries: There is subsegmental pulmonary embolism in both lower lobes.

Lungs and Airways: Emphysema. Mild pulmonary edema. Bibasilar atelectasis. Artifact limits detection for small nodules. 18 mm focal groundglass nodule in the left lower lobe on image 81.

Pleura: Small bilateral pleural effusions. No pneumothorax.

Heart and mediastinum: Mild cardiomegaly. Enlarged main pulmonary artery to 3.4 cm.

Chest Wall and Lower Neck: Normal.

Chest Bones: Status post left thoracotomy.